Journal of Manufacturing Processes 107 (2023) 549–558

Contents lists available at ScienceDirect

Journal of Manufacturing Processes

journal homepage: www.elsevier.com/locate/manpro

In-process non-destructive evaluation of metal additive manufactured components at build using ultrasound and eddy-current approaches

Rastislav Zimermann [a,*], Ehsan Mohseni [a], Euan A. Foster [a], Momchil Vasilev [a], Charalampos Loukas [a], Randika K.W. Vithanage [a], Charles N. Macleod [a], David Lines [a], Misael Pimentel Espirindio E. Silva [b], Stephen Fitzpatrick [b], Steven Halavage [b], Scott McKegney [b], Muhammad Khalid Rizwan [a], Stephen Gareth Pierce [a], Stewart Williams [c], Jialuo Ding [c]

[a] Centre for Ultrasonic Engineering, University of Strathclyde, Glasgow, UK
[b] National Manufacturing Institute Scotland, University of Strathclyde, Glasgow, UK
[c] Welding Engineering and Laser Processing Centre, University of Cranfield, Cranfield, UK

ARTICLE INFO

Keywords:
Wire + arc additive manufacturing
Collaborative robotic cells
In-process non destructive evaluation
Dry-coupled ultrasound testing
Eddy-current testing

ABSTRACT

Metal additive manufacturing is rapidly gaining popularity and interest from sectors aiming to produce larger-scale high-value components cost-effectively. To ensure each component is leaving the fabrication cell defect-free, it is highly desirable to inspect each layer or selected volume of the build. This is a significant challenge, given that conventional non-destructive evaluation (NDE) is a post-manufacturing operation. The opportunity exists in the development of novel flexible automated manufacturing systems aiming to merge deposition and inspection. Hence, enabling defect detection at the point of the creation allows subsequent rapid repair or reduction in scrappage. In this work, the authors present research from one such multi-robot cell, where a directed energy deposition process called wire + arc additive manufacture is used to build components while novel in-process ultrasound and eddy-current approaches are deployed to inspect a component with artificially embedded reflectors. The outcome of this work demonstrates a promising ability to merge manufacturing and NDE into a single process and hence, strengthen the overall benefits of metal additive manufacturing fields.

1. Introduction

Additive Manufacturing (AM) also called three-dimensional (3D) printing is a process of object fabrication using a layer-upon-layer basis, where the deposition paths are driven by digital 3D model Data [1]. As businesses move towards Industry 4.0 [2,3], AM adoption is forecasted to increase through the growing interest in developing smart manufacturing systems capable of fabricating high-quality and high-value customizable products. Sectors, where this capability is most sought after, are aerospace and automotive. This demand can be also expressed by a prediction of market growth in which the metal AM sector is estimated to increase its value by up to 27.9 % annually until 2024 from the original estimated size of 2.02 billion € in 2019 [4].

This paper is associated with one such metal AM technique, called Wire+Arc Additive Manufacturing, which is based on the Directed Energy Deposition (DED) process [5]. WAAM enables the automated production of large high-value 3D near-net-shaped structural engineering components [6] as demonstrated in Fig. 1. The research and development of the WAAM process are targeted to deliver flexible manufacturing with additional benefits of increased cost-effectiveness. This is obtained by reduced material and energy usage as compared to traditional manufacturing such as machining or forging. Hence, technical benefits can enable an economical superiority of WAAM against conventional medium to large-scale manufacturing which is often subtractive, or assembly-based [7].

WAAM has already attracted the attention of aerospace, naval engineering and civil infrastructure due to their growing interest in reducing the weight of products while increasing the possible geometrical complexity of a single part [8]. A clear example has been demonstrated, where WAAM was utilized to build a geometrically complex 6000 kg heavy stainless steel bridge, crossing a canal in Amsterdam (Netherlands), with a width of 2.5 m and a span of 10 m [9]. This project has proved that metal AM can be used as a cost-effective and technically robust substitute for assembly-based construction practices typically

* Corresponding author.
E-mail address: rastislav.zimermann@strath.ac.uk (R. Zimermann).

https://doi.org/10.1016/j.jmapro.2023.10.063
Received 28 August 2023; Received in revised form 16 October 2023; Accepted 25 October 2023
Available online 3 November 2023

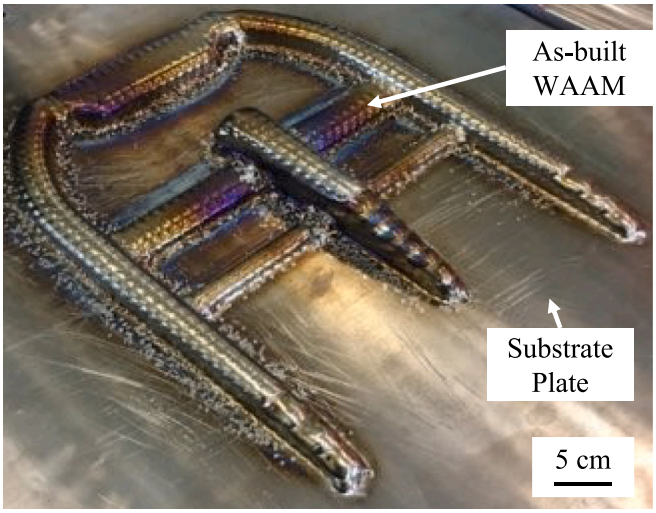

Fig. 1. A complex titanium WAAM component built using an oscillation deposition strategy on a substrate plate.

found in the civil infrastructure industry.

Moreover, the lower waste associated with WAAM amplifies its attractiveness further when energy-intensive alloys, such as titanium [10,11], steel, and nickel-based super alloys [12] are used in a deposition. A strong potential has been demonstrated by the authors [12] who have reported a titanium alloy savings of an estimated 220 kg to manufacture a 24 kg aircraft landing gear assembly. The WAAM process used a deposition rate of ~0.8 kg/h and enabled the efficient manufacture of features such as T-junctions and inclined walls. Traditional subtractive machining operations would have resulted in both time and material waste.

When considering the WAAM process for high-value component production in safety-critical industries such as aerospace or civil infrastructure, the quality and the absence of any flaws must be assured. Component quality is typically assured by Non-Destructive Evaluation (NDE) methods which allow the mechanical quality of the finished component to be assessed before entering service. When considering NDE of WAAM, the most common approaches have been either manual or basic automated post-manufacturing inspection either conducted primarily by ultrasound testing [13], often expensive and hazardous X-Ray based imaging [14], or recently emerging Eddy-Current Testing (ECT) [15]. The post-manufacturing deployment of NDE often creates a bottleneck on the production floor given the necessity to pre-process the parts by transferring them between workstations and performing milling operations to facilitate smooth contact surfaces [14]. These disparate processes of machining and inspecting are undertaken separately and hence, can negatively impact the overall benefits of deploying WAAM for high-value components. Therefore, there is a growing desire to integrate the inspection and manufacturing processes so that defects can be detected at the point of their creation. Such a task can be attained by automatically deploying an in-process NDE. For example, it is common to use robotic arms to deploy the NDE sensors enabling high positional accuracy, good levels of repeatability, high rates of inspection, and the ability to operate in hazardous and hostile environments [16,17].

The in-process inspection of arc-based manufacturing processes and WAAM have been pioneered by [18] and authors' previous work [19–21]. The development of these multi-robot cells demonstrated the possibility of robotic welding and WAAM in combination with automated NDE. Full automation was accomplished by a novel sensor-enabled robotic system based around a real-time embedded controller which enabled: 1) real-time communication, 2) data acquisition and 3) control of the process. Moreover, a UDP (User Datagram Protocol) communication protocol established through the KUKA Robot System Interface (RSI) [22], was used for the robotic motion correction that could influence the pre-programmed robot's path through the sensor feedback. The motion corrections were executed based on innovative robot kinematics software operating in real-time intervals (4-millisecond intervals for KUKA Robot Controller (KRC) 4) [23].

In the context of the in-process inspection of WAAM, a suitable NDE process for robotic deployment capable of withstanding hostile temperatures must be selected. Suitable NDE processes for in-process inspection are well documented in the literature [14,24–26], and it was found that ultrasound and ECT were the best-suited NDE processes for the in-process inspection of WAAM components, due to enhanced sensitivity to a wide range of defects along with a low cost of equipment and simple integration into existing manufacturing environments.

When considering electromagnetic-based inspection techniques, a multiturn coil is excited by alternating voltage to generate alternating currents and a magnetic field around the coil. When the coil is placed in proximity to a conducting sample, The coil's magnetic field interacts with the sample and eddy currents are created within the target. Once the coil is positioned over a surface/subsurface flaw, within the range of eddy currents penetration depth, the current density changes in the sample and that causes a change in the net magnetic flux passing through the inspection coil, which is detected as a change in the coil's impedance [16].

When considering the eddy-current for automated NDE deployment, the opportunity for rapid inspection of either ferromagnetic or non-ferromagnetic and electrically conductive test pieces is enabled [27]. It was demonstrated in the literature that robotic ECT can be deployed for the detection of a matrix of stress corrosion cracks in nuclear canisters [28], where force-torque measuring capabilities enabled sustained contact force for the probe on the specimen along an angular path. Bespoke eddy current probes specifically designed for WAAM cold inspection have also been reported [29]. The coil geometry facilitated the contact to an as-built undulating surface of an aluminium WAAM component and detected 0.35 mm side-drilled holes at depths of 2 mm. Despite the ECT featuring a very high surface/near-surface sensitivity and detectability, the penetration depth depends on the electrical conductivity and magnetic permeability of the test piece and the selected test frequency and is often limited to a few millimeters below the surface. Therefore, in the context of the in-process NDE of WAAM, ECT arrays offer the potential for the online screening of newly deposited upper layers during the manufacturing process [28]. This is due to possible increased surface coverage, conformity to the undulating geometries, enhanced control over the probe's lift-off and tilt as well as possible decreased screening times.

The use of elastic waves emitted by Phased Array Ultrasound Transducers (PAUT) to detect flaws within the volume of metallic components is often among the preferred NDE techniques [30–33]. Moreover, the research has also already presented the possibility of inspecting welds in-process and at elevated temperatures owing to novel dry-coupled PAUT roller-probes [34]. A variant of this roller-probe has also been developed to inspect WAAM layer-by-layer, volumetrically (after every N layer) or in live-arc mode through an as-built surface without the use of liquid coupling [35]. This latter capability enables the inspection of multi-layers simultaneously reducing any time and sunk cost associated with the inspection of high-confidence processes. The WAAM roller-probe, was based on a 0° delay line, the PAUT, and the tire. The design assured full compliance of the roller-probes tire to the non-flat and varying (in both the scanning and the transversal direction) as-built surface of a WAAM component at high force. Hence, the maximum transmission of ultrasound energy into the component was facilitated without minimizing the signal losses caused by low contact quality. From this development, the possibility of detecting a Lack of Fusion (LoF) defects as small as 5 × 0.5 × 0.5 mm (width, length & height), through an as-built surface of the WAAM wall [26] was demonstrated. Moreover, a first in-process NDE of hot and as-built WAAM components with artificial reflectors was conducted as well [18].

In this paper, novel research and developments from the field of in-process inspection of WAAM are presented. First, the authors describe the bespoke cell integrating both WAAM and in-process NDE. For the first time, a hybrid NDE featuring a high-temperature flexible eddy-current array probe and high-temperature dry-coupled ultrasound roller-probe were integrated and deployed on as-built titanium WAAM straight component at elevated temperatures. Both methods were deployed during a dwell time, set for inter-layer cooling, while sufficient coupling force between NDE sensors and the as-built surface of WAAM during the inspection was assured by a 6-axis robotic arm with force torque feedback. To assess the inspection capabilities of the two approaches, a Ti-6Al-4 V WAAM straight component (wall) with various embedded tungsten reflectors was deposited. The use of tungsten tubes as artificial reflectors for both ultrasonic calibration and defect detection has been documented for in-process weld inspection [19,20]. The embedding of tungsten tubes or balls allows the controlled creation of inclusions with known sizes and shapes at the predetermined location within the part. This is particularly true for tungsten balls application in eddy-current experiments where the contrast in electrical conductivity between titanium and tungsten is ~6.9 MS/m while between air and titanium, it is 2 MS/m [36,37].

Throughout the experiment, ECT was used to inspect 'defective' WAAM layers after they were deposited due to its limited penetration depths expected to reach only a few millimeters below the surface (in Ti-6Al-V the standard depth of penetration equals ~1.3 mm according to [38]). Subsequently, a bespoke dry-coupled ultrasonic roller-probe enabling layer-by-layer and volumetric imaging was deployed in the latter configuration due to the relatively low wall height of the component, to conduct an in-process inspection. In both scenarios, the position-encoded inspection data were acquired and presented on an amplitude C-scan image [39]. Two different eddy current datasets (axial and transversal) corresponding to different transmit and receive topography were analyzed and compared. For the ultrasound inspection, two approaches were repeated. First, the live-beamforming-inspection with a fixed-depth focus was deployed to produce an interior image of the WAAM component [40]. The inspection was then repeated to acquire ultrasound Full Matrix Capture (FMC) data and to post-process it later using the Synthetic Aperture Focusing Technique surface finding and Total Focusing Method (SAFT-TFM) imaging package [26]. Finally, produced C-scans were plotted and cross-comparison of both ECT and ultrasound inspection approaches was conducted.

2. WAAM & NDT cell

2.1. Plasma wire + arc additive manufacturing

In this work, the experimental specimen was manufactured in the cell introduced in the author's previous work [18] where the automated WAAM hardware, depicted in Fig. 2, is developed around a 6 Degrees of Freedom (DoF) industrial robotic arm (KUKA KR90 R3100) capable of handling the WAAM deposition activity within the cell. The components were built on a substrate plate clamped to the horizontal rotary positioner (KUKA DKP-400 V3) also located within this cell. The specimen was deposited by the deposition head featuring a water-cooled plasma-arc welding torch (controlled by: EWM-TETRIX 552 AC/DC SYNERGIC PLASMA AW welder) integrated into a deposition device with a local shielding, and it was mounted on the end effector of the KUKA robot [41], as seen in Fig. 2. The local shielding device (WAAM3D, UK) was an aluminium enclosure, containing additional gas outlets, supplying the argon shielding gas on a high-temperature WAAM and hence preventing the atmospheric contamination that could result in oxidation of the fresh deposit. Further, a wire-feed outlet with adjustable height was mounted to the deposition device and set to supply feedstock directly into the melt pool. The wire supply was provided by a wire feeder (EWM T drive 4 Rob 3 Li, EWM) that was attached directly to the deposition robot's arm as well. Lastly, the melt pool and the deposition were monitored using a high dynamic range welding camera (Xiris XVC-1000).

2.2. In-process inspection

An inspection robot (also Kuka KR-90-3100), seen in Fig. 3, was located opposite the deposition robot within the same cell, however, this robot was equipped with a Force/Torque (FT) sensor (FTN-GAMMA-IP65 SI-130-10, ATI Industrial Automation (Apex, NC, USA)) mounted on the end effector. The NDE was then accomplished by two approaches. The ultrasound NDE approach was based on a high-temperature dry coupled WAAM roller-probe (resistant to 350 °C). The roller-probe was driven by a high-speed phased array ultrasound controller LTPA (PEAK,

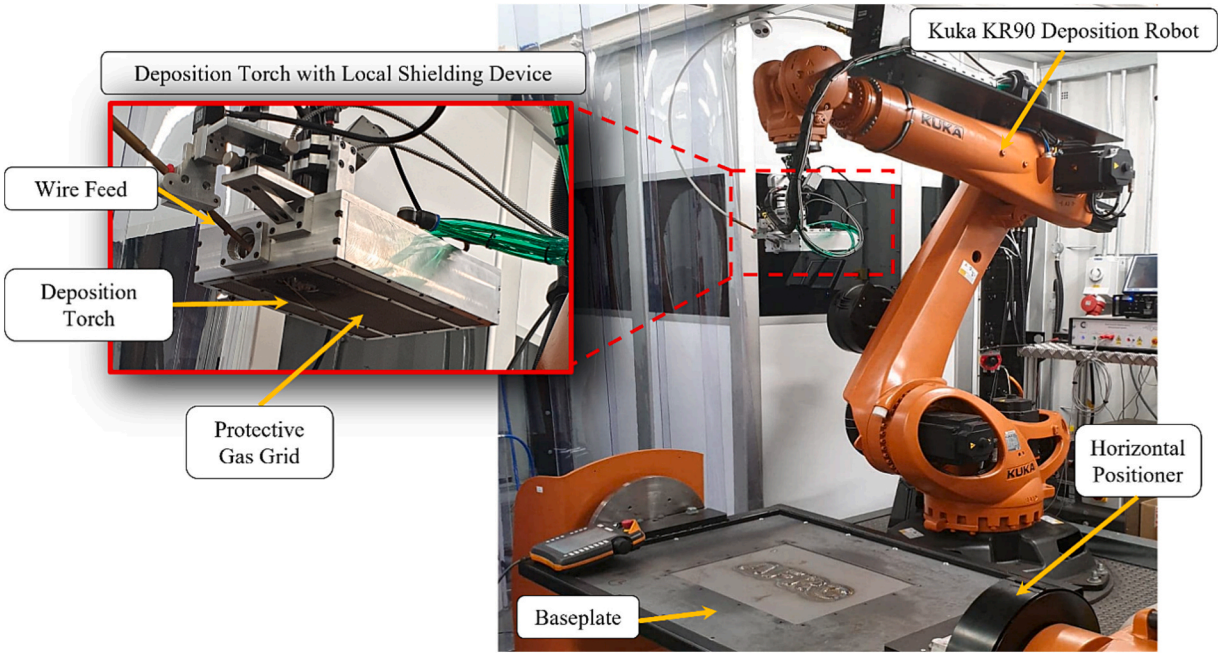

Fig. 2. WAAM deposition robot featuring a plasma arc process.

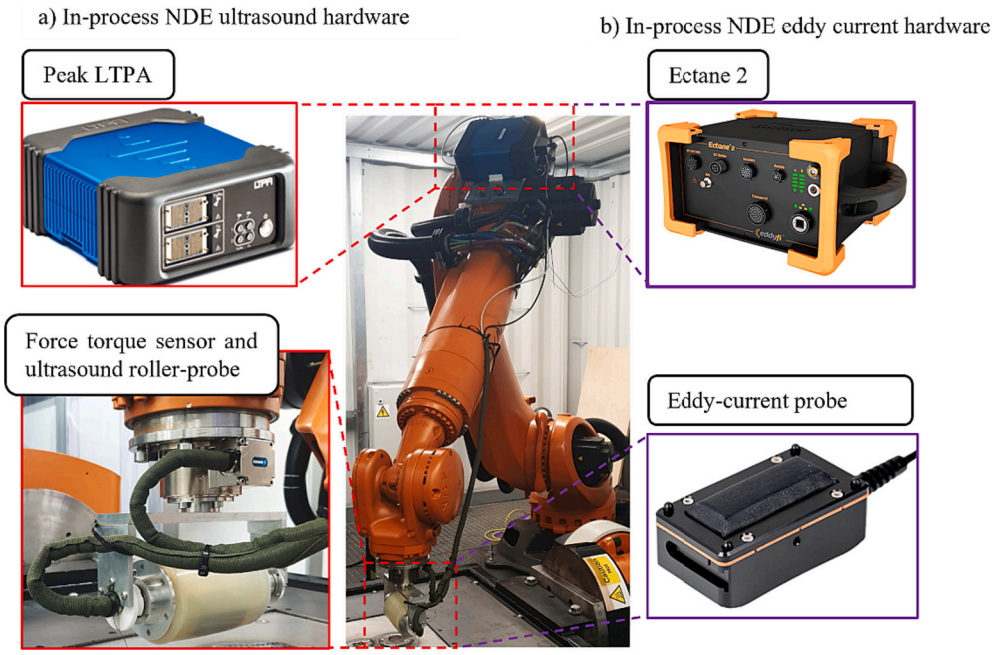

Fig. 3. In-process NDT setup carrying ultrasound and ECT equipment.

NDT) mounted directly on the robot arm. The second approach included a padded flexible EC probe which was driven by an EC controller (Eddyfi Technologies, Canada). The padded flexible EC probe enabled coupling with an as-built WAAM component at a temperature of 150 °C for up to 30 s. Further, the communication between all hardware was achieved by Zyxel Gigabit ethernet enabling control of the presented system.

During the experiments, the deposition robot was controlled by a pre-installed PC with a WAAMCtrl (WAAM3D, UK) [42] application, streaming the deposition commands (robot paths, deposition parameters) directly to the deposition robot via RSI over an ethernet connection. The tool-path plan was generated using WAAMPlanner Software (WAAM3D, UK) [43], where the desired component was imported as a Computer-Aided Design (CAD) file, sliced into layers according to the pre-defined layer height, segmented into a set of individual building blocks from which the series of tool-paths was generated.

The robotic NDE inspection was guided by a software platform developed in the LabVIEW programming environment [44]. During both ECT and ultrasound inspection, the inspection parameters were sent to the controllers through the LabVIEW program as indicated in the diagram in Fig. 4. The acquired data (ultrasound and eddy current) were then paired with the robot position stamp and stored on the hard drive for later post-processing. Positionally accurate C-scan displays were accomplished using MATLAB for the ultrasonic data and LabVIEW for the eddy current data.

3. Experimental specimen manufacturing

3.1. Experimental WAAM deposition

A manufactured, straight titanium (Ti-6Al-4 V) WAAM wall formed the foundation for the experimental work intended to assess and demonstrate the in-process inspection capacity of the ECT system and dry-coupled ultrasound roller-probe system. The specimen's measurements were fixed at 25.0 mm in width, 300.0 mm in length, and 25.0

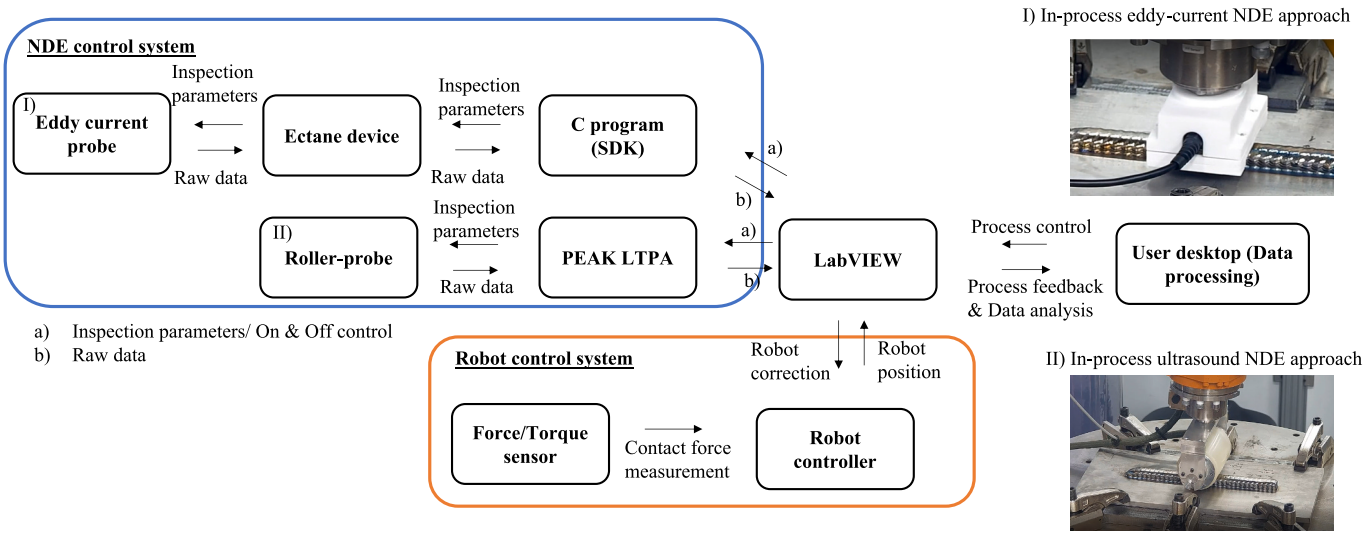

Fig. 4. Diagram of NDE software driving the process.

mm in height. However, given the WAAM technique's capacity to make components with an overbuilt close to a net shape, excess material accumulated on the edges was anticipated. [12].

The path planning designed in WAAMPlanner, seen in Fig. 5, consisted of an oscillating deposition strategy [45], where a single bead, with a square zig-zag pattern, was deposited per layer. Relevant deposition parameters can be seen in Table 1 below.

Fig. 6 shows an experimental deposition setup where a Ti-6 V-4AL specimen was deposited on a substrate plate that was 12 mm thick and fastened to the tooling, in this case, a set of welding clamps that kept the plate fixed to the horizontal positioner. Additionally, the welding clamps made it easier to prevent plate distortion caused by heat-induced residual stresses [46], which is common in arc-based manufacturing processes like welding [47]. Fig. 6 (a) also shows the active deposition of the first layer, while Fig. 6 (b) displays the finished pass 1. It is important to note that the layer height was determined to be consistent at about 3.5 mm.

3.2. Artificial defect embedding for NDE experiments

To assess the effectiveness of the NDE flaw-detecting capacity, artificial reflectors were incorporated into the experimental wall. The tungsten tubes with the specifications listed in Table 2 were initially inserted into layer 3. A portable grinding machine was used for the embedding, creating pockets that held the tungsten tubes in place during the subsequent deposition. The distance between the tubes was roughly 55 mm. A longitudinally positioned tube (WT-L) was positioned in the middle of the bead, roughly parallel to the wall. Fig. 7 depicts how the Tube (WT-T) was inserted into the wall transversely. Following the deposition of layer 4 covering the tungsten tubes, the additional tungsten balls with diameters 3 mm (WB-3) and 2 mm (WB-2) were embedded into the WAAM using the same technique as also seen in Fig. 7.

4. In-process inspection

4.1. Experimental work strategy

The in-process inspection capabilities in this work were demonstrated during a dwell time that was designated for interlayer cooling. Shortly after the torch stopped depositing layers 4 and 5, ECT was performed. As a result, the detection of tungsten tubes (included in layer 3) and tungsten balls (incorporated in layer 4) was carried out immediately following their recent titanium deposition. After pass 5's ECT inspection was completed, layer 6 was deposited after the end-effector was altered for the dry-coupled ultrasonic roller-probe. The experimental work was completed with live ultrasound beamforming imaging, and ultrasound in-process inspection was repeated with FMC data collection for post-processing using the SAFT-TFM imaging approach.

Table 1
Deposition Parameters.

Deposition parameters	
Current	150 Amps
Wire-feed speed	2.5 m/min
Robot Velocity	0.005 m/s

As mentioned, the inspection was carried out within a dwell time, which in this work was set to 9 min. As suggested by the literature [32], this cooling period was found optimal to avoid the formation of phase αGB grain microstructure [48] in Ti-6Al-4 V walls built using oscillation deposition strategies.

The approach for sensor-driven robotic NDE, used in this work, was presented by [18,28], where the Force/Torque sensor data facilitated the robot position correction maintaining the desired contact force and orientation between the NDE sensor and the test component. The intelligent triggers, programmed within LabVIEW, were used to automatically enable and disable features such as the sensor/path-driven motion, inspection data acquisition and data handling.

Given the maximum operating temperature (<150°) of ECT equipment, before every inspection, the surface temperature of the built WAAM wall was monitored using a hand-held thermometer. Once the surface temperature was within the limit (measured within 3 min), the ECT was initiated. During the inspection, the robot speed was set to 0.015 m/s at the 30 N of force applied to the component. This force set was found to sufficiently press the probe's padding around the top surface of WAAM without damaging or tearing itself. Despite the ability of the probe's padding to conform to the surface of the WAAM, the overall scan length of 250 mm was targeted, avoiding the corners where possible spatter from arc ignition and cut-off could occur and tear the probe's padding. The total inspection time was approximately 17 s with an additional approximately 1 min taken for the robot to approach and retract from the specimen.

Finally, the in-process inspection was conducted by employing the dry-coupled ultrasound roller-probe targeting the WAAM volume between a fresh layer (pass 6) and a substrate plate interface. This was achieved after the layer 6 deposition, where at first the surface temperature was measured and ranged to be between 180 and 230 °C, which was much lower than the maximum operating temperature limit of the roller-probe (resistant up to 350 °C). Thus, the inspection was initiated within the first 2 min of the dwell time where the inspection pass was repeated twice to collect both FMC and live beamforming data respectively. During the inspection, the robot speed was set to 0.002 m/s at a force of 130 N. The inspection duration was therefore 125 s to inspect a 250 mm long volume and just over 3 min to complete both inspection passes. It is worth noting that despite repeating the inspection twice, the overall inspection time was much lower than the minimum 9-min-long dwelling time set for interlayer cooling in case of hypothetical

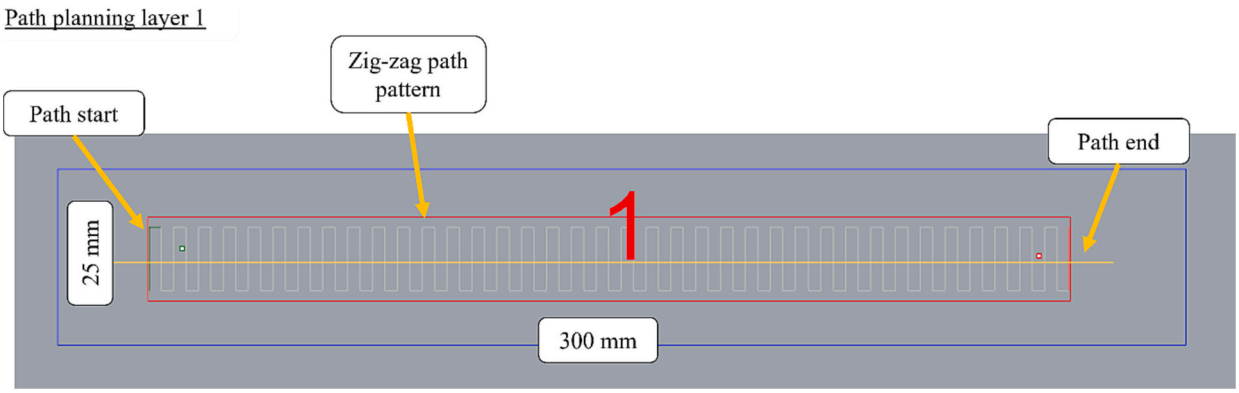

Fig. 5. Deposition path planning for layers of an experimental WAAM wall.

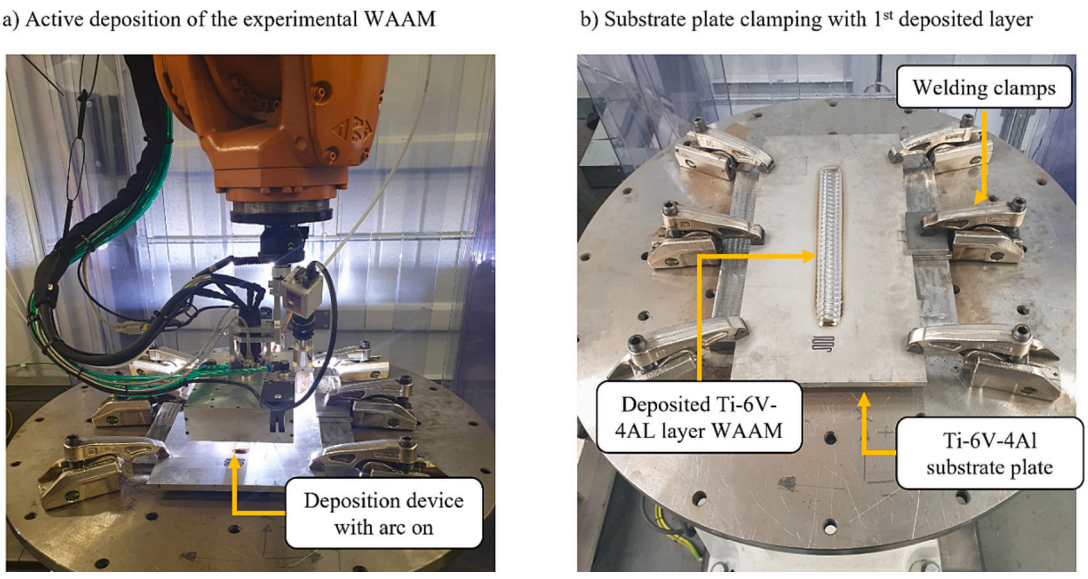

Fig. 6. Deposition clamping setup and a substrate plate with a deposited 1st layer (left) and deposition process with an active torch (right).

Table 2
Tungsten tube parameters.

Tungsten tube	
Tube length	30 mm
Internal diameter	1 mm
Outer diameter	3 mm

subsequent deposition.

Once the manufacturing and experimental part of the work were completed, the sample was subjected to an X-ray computer Tomography (XCT) to validate the presence and location of embedded reflectors along with possible process natural defects. The X-ray CT was conducted using a Nikon XT H 225/320 LC X-ray computer tomography system fitted with a 225 kV X-ray source. Given the distance of the sample from the X-ray source, a maximum resolution of 100 μm was achieved.

4.2. Eddy current in-process NDE of as-built WAAM

4.2.1. Eddy current experimental parameters

The padded probe, specified in Table 3, was directly coupled to the as-built surface of WAAM. As mentioned previously, this custom-built probe could withstand a maximum operating temperature of up to 150 °C for up to 30 s.

During the inspection, the data acquisition rate was set to 500 Hz, while the data were acquired with 40 dB of gain and a voltage excitation of 2.5 V. The collected signals corresponding to 50 kHz were stored and displayed on C-scan images plotted using axial and transversal elements respectively.

4.2.2. In-process eddy-current NDE after layer 4

The resulting eddy-current C-scan images from the inspection after pass 4 can be seen in Fig. 8. The detection of tungsten tubes was best visible when plotting the results using an axial group of elements at 145° phase rotation, as seen in Fig. 8 (a). Both WT-L and WT-T tubes were detected, however, the representation of WT-L was continual while WT-T was mainly detected at its edges. Comparing the detection to the presented XCT image, a close agreement with the EC results in terms of location and orientation was observed. Fig. 8 (b) displays the results

Table 3
Eddy current array configuration.

Central frequency	50 kHz
Frequency range	15 kHz – 250 kHz
Coil quantity	32
Coil layout	2 rows of 16 coils
Coil type	Pancake

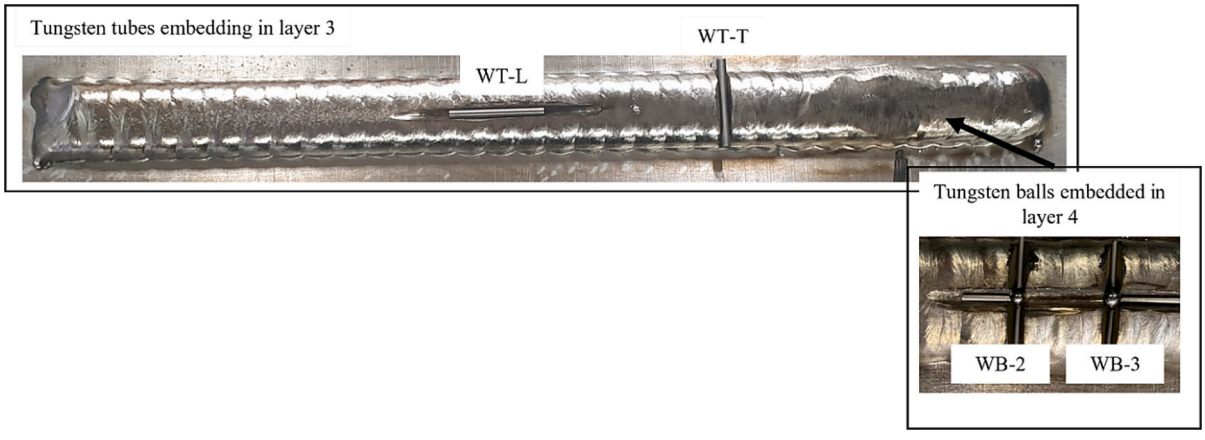

Fig. 7. Tungsten reflectors embedded into the experimental WAAM.

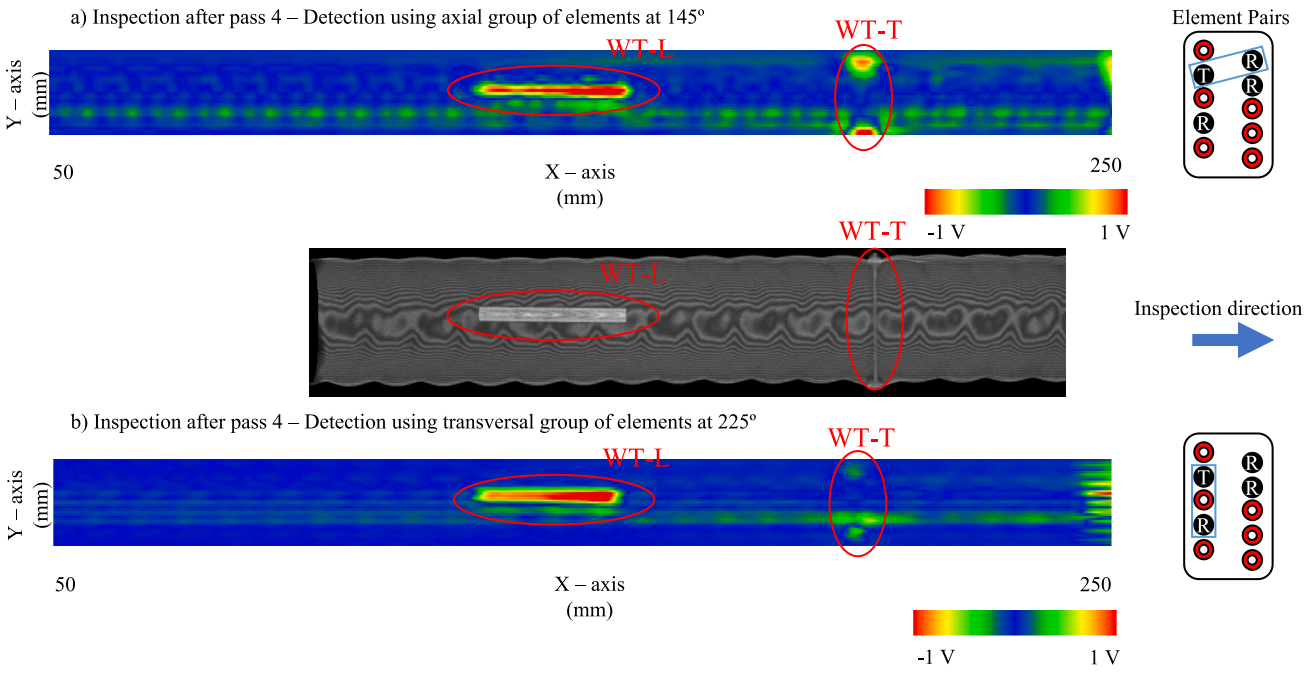

Fig. 8. Eddy-current inspection results after layer 4.

when using a transversal group of elements where the defects were best visible at 225° phase rotation. Similarly, WT-L was clearly detected in agreement with the XCT image while WT-T produced a much weaker signal when compared to the detection using an axial group of elements.

4.2.3. *In-process eddy-current NDE after layer 5*

The eddy current inspection of the build volume after layer 5 was targeted at the possible detection of tungsten tubes as well as tungsten balls embedded into layer 4. From the images in Fig. 9, it was clear that TW-L, as well as transverse WT-T, were no longer detected, given their depth of ~ 8 mm. It is worth noting that at a depth of ~4.5 mm in

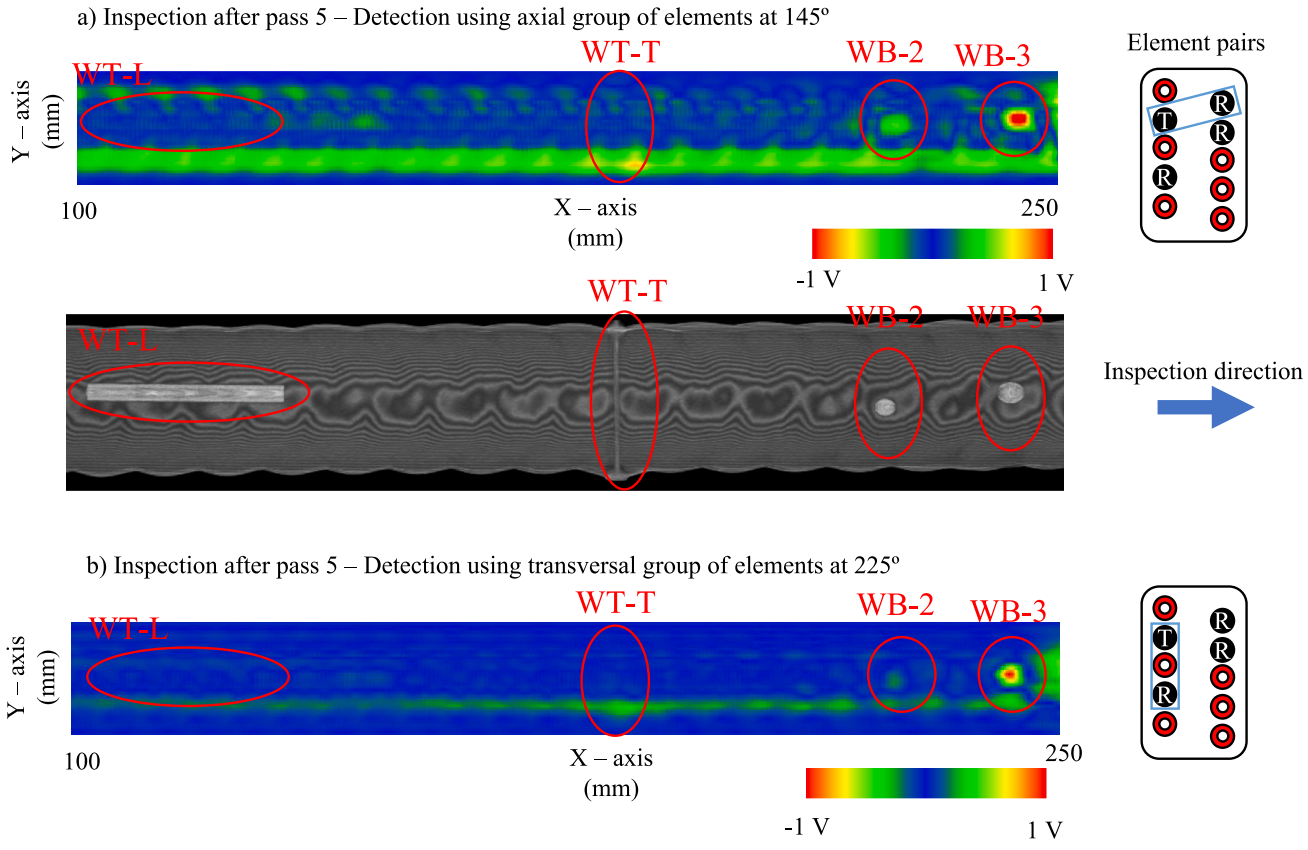

Fig. 9. Eddy-current inspection results after layer 5.

titanium the eddy current density is 95 % lower than its surface value at a frequency of 50 kHz. The exponential decay of the current density as a function of inspection depth explains the decreased detection ability of the tungsten tubes after the subsequent deposition. On the other hand, the tungsten balls were strongly visible, and WB-3 had a more significant appearance in the image when compared to its WB-2 counterpart. When comparing Figs. 9 (a) and (b) where the images were plotted using an axial and transversal group of elements respectively, the appearance of tungsten balls was seen with a comparable signal level above the noise level. Moreover, no further defects were detected by the ECT system during the in-process NDE.

4.3. Dry-coupled ultrasound roller-probe inspection

4.3.1. Ultrasound inspection parameters

The ultrasound data was acquired using a roller-probe featuring a 26 mm high solid delay line housed in a 6 mm thick silicone rubber tire. The PAUT, with specifications found in Table 4, was positioned to sit on the top of the delay line.

At first, the inspection was conducted using conventional ultrasound beamforming focusing techniques, which offered the benefit of live data visualization. During the data acquisition, the 32-element sub aperture with 1-element shift was focused into layer 3 to inspect the location of the tungsten tubes at the centre of the deposited volume. During the inspection, the sub-aperture excitation was accomplished using 200 V and 50 dB of hardware gain. The B-scans obtained during the inspection were saved on a local hard drive at the frequency of 6 samples/mm, post-processed to feature WAAM interior only and displayed on an amplitude C-scan image. The C-scan was produced from all frames by selecting the highest amplitude value from each A-scan. The image was then normalized to the highest value of the newly formed C-scan and displayed on a decibel scale from 0 to −20 dB.

The inspection was also repeated acquiring the FMC data using ultrasound parameters of 200 V, 100 ns pulse excitation voltage and a fixed hardware gain of 60 dB. The time-domain matrix of the signals was formed by 3000 data samples for each transmit-receive pair at a sampling frequency of 50 MHz. During the inspection 150 FMC frames were acquired, giving a density of 1.7 samples/mm. The data was processed using the following acoustic velocities for longitudinal ultrasound waves: 1) Delay line = 2480 m/s, 2) Rubber = 1006 m/s and 3) Titanium = 6100 m/s [18].

After the completion of the FMC data acquisition, the ultrasound data collected during the inspection was processed using the SAFT-TFM algorithm described in the author's previous work [26]. In this work, signals corresponding to the centre 32 elements of transmitters and receivers forming FMC data were deployed to form final images. This was due to the size of the array being much larger than the width of the sample (~25 mm). Hence, the contribution of the corner elements towards the imaging of the WAAM interior would mainly consist of noise and false echoes. The TFM frames were computed for a 25 mm × 19 mm region at 6 pixels/mm resolution, which was compatible with the 2 dB Amplitude Fidelity criterion of ASME V [49]. This window represented an internal volume of the desired component between the baseplate and beneath the surface just above the interface of layers 5 and 6.

To achieve a full C-scan, the computation was initiated by the ultrasound surface reconstruction using an SAFT surface imaging and surface finding algorithm [26]. Afterwards, the curves representing the WAAM surface contours were augmented into the 3-layer adaptive TFM algorithm to produce the TFM frames before their normalization, using the centre 48 elements of the PAUT probe. The corner 8 elements of the phased array were excluded from the computation given their location outside of the component's surface which would result in higher noise and false signal contribution negatively affecting the SNR. The final C-scan image was then created using 150 × 200 pixels (Number of pixels in the horizontal axis of the TFM frame × the number of frames) normalized and plotted on a dB scale ranging from the peak amplitude value to the average noise level (0 to −20 dB).

Table 4
PAUT parameters.

Array parameters	Value
Element count	64
Element pitch	0.5 mm
Element elevation	10 mm (unfocused)
Element spacing	0.1 mm
Centre frequency	5 MHz

4.3.2. Results of dry-coupled ultrasound roller-probe in-process inspection of WAAM volume

In this section, the results of dry-coupled in-process ultrasound NDE of a WAAM wall interior volume are presented and discussed. At first inspection results featuring live beamforming focusing and SAFT-TFM applied for volumetric imaging of the WAAM interior were displayed in Fig. 10 (a, b). Successful detection of WT-L and TW-T was achieved along with a strong presence of signals retrieved from the location of the tungsten balls WB-2 and WB-3. It is noteworthy, that the tungsten balls were not suitable reflectors for ultrasound given the lack of air/material interface. However, as soon as these balls were embedded, a range of natural defects such as porosity and Lack of Fusion (LoF), explaining these retrieved signals, were produced.

Therefore, to validate the ultrasound indications from inspection, Fig. 10 (c) was generated to depict the interior of WAAM at the location of the tungsten balls using XCT. From the figure, the presence of porosity and lack of fusion defects around tungsten balls were observed. A significant porosity cluster (P) depicted in Fig. 10 (c) was located just on the left-hand side of the WB-3. Closer analysis of this location revealed the presence of pores with the most significant defect as big as 0.5 mm in diameter and 0.6 mm in length and with additional pores with a size of around 0.2 mm in diameter. Further, when reviewing the detected signals directly from the location around WB-2 and WB-3, the presence of natural defects (air pockets) was observed. These LoF cavities were created during tungsten embedding where the unmelted tungsten did not fuse to the titanium due to its much larger melting point (~3400 °C) as compared to titanium alloy (~1600 °C). It is worth noting that the detection of defects in very close proximity to the tungsten was extremely challenging for the XCT due to the large density of tungsten (19.3 Mg/m3), which acted as a radiation shield during the scan.

To quantify the results, an SNR of up to 20 dB and 18 dB was achieved from the WT-L when using both SAFT-TFM and conventional electronic beamforming respectively. Further, a similar SNR was retrieved from WT-T during the electronic beamforming scan, while a 10 dB SNR was achieved by the SAFT-TFM during the inspection. Despite the tungsten balls not being planted as an ultrasound-friendly reflector, the signals from LoF and porosity defects, created during tungsten embedding, were detected with a range between 5 and 10 dB using both ultrasound imaging techniques.

In both inspection scenarios, the fluctuation of the SNR along the signal corresponding to WT-L was notably visible, where the SNR was seen to drop by up to 10 dB. This reduction in signal amplitude is associated with a highly undulating surface of the as-built. Furthermore, the authors associate the additional signal losses due to non-uniform wave velocity within the component due to thermal gradient [19].

4.4. Comparison of in-process NDE approaches

In this section, the key findings from the inspection results were summarized and compared. First, it must be noticed that ECT offers great potential for the short, up to 30-s inspection with a maximum operating temperature of 150 °C) of fresh layers due to surface and near-surface sensitivity. However, as soon as the inspection delivery becomes a constraint and a volumetric inspection is required (every n layer), the

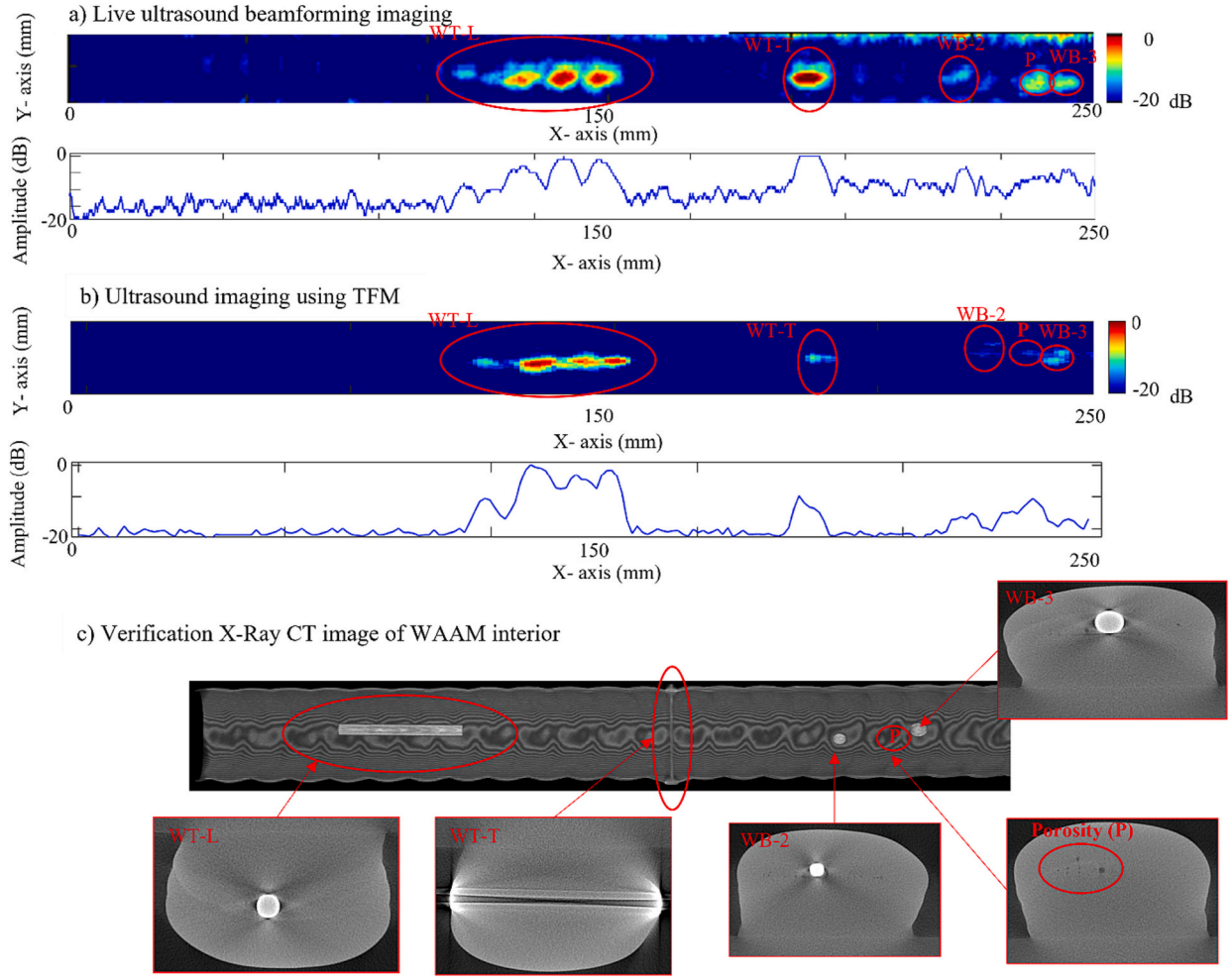

Fig. 10. Shows (a) a C-scan using conventional beamforming imaging, (b) a C-scan built from FMC-based SAFT-FTM imaging and (c) a verification XCT image of WAAM Interior.

dry-coupled ultrasound roller-probe approach provides a potential for layer-by-layer or volumetric and bulk inspection of as-deposited components owing to its temperature resistance up to 350 °C without the need for a cool-down period due to optional active cooling hardware.

When considering the ECT and dry-coupled ultrasound for industrial applications, the size and the speed of data processing must be considered. As discussed in the author's previous work [18,26,50], ultrasound data acquisition methods such as FMC with the following 3-layer adaptive TFM post-processing demand large data storage capacity and computational power which will require higher initial equipment cost. In this paper, the ultrasound data post-processing was accomplished using AMD Ryzen Threadripper 3960 24-core Processor with a clock speed of 3.79 GHz and 128 GB of Random-Access Memory. A full set of ultrasound FMC data was around 1 gigabyte in size and the time elapsed to compute a single SAFT-TFM frame was measured at 75 s. In the case of eddy-current data processing a C-scan plotting, the data size was found to be around 16 megabytes, while the display of the results was live and required manual phase rotation adjustments to optimize the data visualization.

5. Conclusions and future work

In this paper, the authors presented the work from the dedicated WAAM & in-process NDE with integrated ECT and ultrasound approaches. At first, the architecture of this manufacturing system was explained, where the plasma arc deposition was mounted on the KUKA robot to deposit near-net-shape components. On the other side, the in-process NDE was facilitated by the deployment of a custom-designed flexible ECT-padded probe and novel high-temperature dry-coupled ultrasound roller-probe. The in-process inspection experiments were delivered on a deposited Ti-6Al-4 V WAAM wall with embedded tungsten tube reflectors (into layer 3) in two directions (longitudinal and transversal) and tungsten balls embedded in layer 4. At first, the ECT was deployed to inspect the built volume after pass 4, targeting the tungsten tube reflectors. The in-process inspection was repeated after layer 5 targeting the detection of additional tungsten balls. Once layer 6 was deposited, the in-process NDE was conducted using an ultrasound phased-array probe targeting not just the freshest layer but the whole WAAM volume using live beamforming imaging and FMC-based SAFT-TFM.

The results of this work showed the successful detection of artificial tungsten reflectors by the ECT when located as deep as the second uppermost layer (up to 4.5 mm deep) but natural defects detected by verification XCT (porosity) remained undetected. On the other hand, full volumetric inspection using the bespoke ultrasound roller-probe demonstrated successful detection of artificial reflectors along with additional detection of both natural lack of fusion defects and porosity clusters with pores ranging from 0.1 to 0.6 mm in diameter.

From the results, it can be concluded that the eddy-current equipment is best suited for the rapid inspection conducted between every layer if it is required, while the dry-coupled ultrasound roller-probe can be also deployed volumetrically or to follow a live-arc deposition torch

due to its long operational cycles.

In future work, authors seek to further develop inspection calibration and in-process NDE strategies for the inspection of complex WAAM shapes and features e.g. joints, curves and varying thickness shapes. In addition, process optimization and evaluation for materials such as aluminium, and steel alloys will be conducted. Further, the authors intend to investigate combined ECT and ultrasound NDE to leverage the strengths of both approaches e.g. surface defects sensitivity of ECT and the volumetric range of ultrasound.

Declaration of competing interest

The authors declare that they have no known competing financial interests or personal relationships that could have appeared to influence the work reported in this paper.

Acknowledgements

The project was supported by EPSRC: (I) NEWAM (EP/R027218/1). Further, the authors would like to thank the technical staff at the National Manufacturing Institute Scotland (NMIS) (Renfrew, UK) for the support of this work, and the team at KUKA Robotics (Jeff Nowill, Alan Oakley, Steve Hudson in particular) for enabling and supporting the robotics work.

References

[1] Kotadia H, Gibbons G, Das A, Howes P. A review of laser powder bed fusion additive manufacturing of aluminium alloys: microstructure and properties. Addit Manuf 2021;46:102155.
[2] Bhatt PM, Malhan RK, Shembekar AV, Yoon YJ, Gupta SK. Expanding capabilities of additive manufacturing through use of robotics technologies: a survey. Addit Manuf 2020;31:100933.
[3] Lima AL, et al. Oscillatory shear rheology as an in-process control tool for 3D printing medicines production by fused deposition modeling. J Manuf Process 2022;76:850–62.
[4] Metal additive manufacture market. https://additive-manufacturing-report.com/additive-manufacturing-market/ (accessed 17/01/2022).
[5] Alhakeem MM, Mollamahmutoglu M, Yilmaz O, Bol N, Kara OE. A deposition strategy for wire arc additive manufacturing based on temperature variance analysis to minimize overflow and distortion. J Manuf Process 2023;85:1208–20.
[6] Hu Y, Chen F, Cao S, Fan Y, Xie R. Preparation and characterization of CMT wire arc additive manufacturing Al-5% Mg alloy depositions through assisted longitudinal magnetic field. J Manuf Process 2023;101:576–88.
[7] Wu B, et al. A review of the wire arc additive manufacturing of metals: properties, defects and quality improvement. J Manuf Process 2018;35:127–39.
[8] Thapliyal S. Challenges associated with the wire arc additive manufacturing (WAAM) of aluminum alloys. Mater Res Express 2019;6(11):112006.
[9] MX3D unveils its additively manufactured bridge in Amsterdam. metalAM.com; 2021. https://www.metal-am.com/mx3d-unveils-its-additively-manufactured-bridge-in-amsterdam/ (accessed 1.9., 2022).
[10] Kennedy JR, Davis A, Caballero A, Williams S, Pickering E, Prangnell P. The potential for grain refinement of Wire-Arc Additive Manufactured (WAAM) Ti-6Al-4V by ZrN and TiN inoculation. Addit Manuf 2021;40:101928.
[11] Yu L, Chen K, Zhang Y, Liu J, Yang L, Shi Y. Microstructures and mechanical properties of NiTi shape memory alloys fabricated by wire arc additive manufacturing. J Alloys Compd 2022;892:162193.
[12] Williams SW, Martina F, Addison AC, Ding J, Pardal G, Colegrove P. Wire+ arc additive manufacturing. Mater Sci Technol 2016;32(7):641–7.
[13] Vasilev M, et al. Non-contact in-process ultrasonic screening of thin fusion welded joints. J Manuf Process 2021;64:445–54.
[14] Lopez A, Bacelar R, Pires I, Santos TG, Sousa JP, Quintino L. Non-destructive testing application of radiography and ultrasound for wire and arc additive manufacturing. Addit Manuf 2018;21:298–306.
[15] García-Martín J, Gómez-Gil J, Vázquez-Sánchez E. Non-destructive techniques based on eddy current testing. Sensors 2011;11(3):2525–65.
[16] Urhal P, Weightman A, Diver C, Bartolo P. Robot assisted additive manufacturing: a review. Robot Comput Integr Manuf 2019;59:335–45.
[17] Kaczmarek M, Piwakowski B, Drelich R. Noncontact ultrasonic nondestructive techniques: state of the art and their use in civil engineering. J Infrastruct Syst 2017;23(1):B4016003.
[18] Zimermann R, et al. Collaborative robotic wire+ arc additive manufacture and sensor-enabled in-process ultrasonic non-destructive evaluation. Sensors 2022;22(11):4203.
[19] Javadi Y, et al. In-process calibration of a non-destructive testing system used for in-process inspection of multi-pass welding. Mater Design 2020;195:108981.
[20] Javadi Y, et al. Continuous monitoring of an intentionally-manufactured crack using an automated welding and in-process inspection system. Mater Design 2020:108655.
[21] Javadi Y, et al. In-process inspection of multi-pass robotic welding. In: Review of progress in quantitative nondestructive evaluation; 2019.
[22] KUKA.RobotSensorInterface 4.0. 2018. https://www.kuka.com/en-gb/products/robotics-systems/software/system-software/kuka_systemsoftware (accessed 19/01/2022).
[23] Vasilev M, et al. Sensor-enabled multi-robot system for automated welding and in-process ultrasonic nde. Sensors 2021;21(15):5077.
[24] Chabot A, Laroche N, Carcreff E, Rauch M, Hascoët J-Y. Towards defect monitoring for metallic additive manufacturing components using phased array ultrasonic testing. J Intell Manuf 2020;31(5):1191–201.
[25] Gao P, Wang C, Li Y, Cong Z. Electromagnetic and eddy current NDT in weld inspection: a review. Insight: Non-Destr Test Cond Monit 2015;57(6):337–45.
[26] Zimermann R, et al. Multi-layer ultrasonic imaging of as-built wire + arc additive manufactured components. Addit Manuf 2021:102398. 2021/10/13/, https://doi.org/10.1016/j.addma.2021.102398.
[27] Kim J, Ju SH, Nam J, Kuttolamadom M, Lee C. Non-destructive surface and subsurface characterization of the machined parts by using fiber optic Eddy current sensor. J Manuf Process 2023;95:492–6.
[28] Foster EA, et al. Automated real-time eddy current array inspection of nuclear assets. Sensors 2022;22(16):6036.
[29] Bento JB, Lopez A, Pires I, Quintino L, Santos TG. Non-destructive testing for wire+ arc additive manufacturing of aluminium parts. Addit Manuf 2019;29:100782.
[30] Drinkwater B, Cawley P. An ultrasonic wheel probe alternative to liquid coupling. 1994.
[31] Lopez AB, Santos J, Sousa JP, Santos TG, Quintino L. Phased array ultrasonic inspection of metal additive manufacturing parts. J Nondestruct Eval 2019;38(3):62.
[32] Mohseni E, et al. Ultrasonic phased array inspection of wire plus arc additive manufactured (WAAM) titanium samples. In: 58th Annual British Conference on Non-Destructive Testing; 2019.
[33] Willcox M, Downes G. A brief description of NDT techniques. Toronto: NDT Equipment Limited; 2003.
[34] Vithanage RK, et al. A phased array ultrasound roller probe for automated in-process/interpass inspection of multipass welds. IEEE Trans Ind Electron 2020;68.
[35] Vithanage RK, et al. Development of a phased array ultrasound roller probe for inspection of wire+ arc additive manufactured components. J Manuf Process 2022;80:765–74.
[36] K. Murthi. Does tungsten conduct electricity? 11 facts you should know. Keerthi Murthi. https://lambdageeks.com/does-tungsten-conduct-electricity/#:~:text=The%20electrical%20conductivity%20of%20tungsten%20is%20approximately%20measured%20as%208.9,a%20good%20electrical%20conductive%20value. (accessed 2022).
[37] Pergament A, Stefanovich G, Berezina O, Kirienko D. Electrical conductivity of tungsten doped vanadium dioxide obtained by the sol–gel technique. Thin Solid Films 2013;531:572–6.
[38] Mottl Z. The quantitative relations between true and standard depth of penetration for air-cored probe coils in eddy current testing. NDT Int 1990;23(1):11–8.
[39] Mineo C, et al. Flexible integration of robotics, ultrasonics and metrology for the inspection of aerospace components. In: AIP conference proceedings. vol. 1806, no. 1. AIP Publishing LLC; 2017. p. 020026.
[40] Ghorayeb SR, Lord W, Udpa SS. Application of a beamforming technique to ultrasound imaging in nondestructive testing. IEEE Trans Ultrason Ferroelectr Freq Control 1994;41(2):199–208.
[41] Xu X, Ding J, Ganguly S, Diao C, Williams S. Preliminary investigation of building strategies of maraging steel bulk material using wire+ arc additive manufacture. J Mater Eng Perform 2019;28(2):594–600.
[42] WAAMctrl. https://waam3d.com/software/control-suite (accessed 18/01/2022).
[43] WAAMPlanner. https://waam3d.com/software/planner (accessed 17/01/2022).
[44] What is LabVIEW?. https://www.ni.com/en-gb/shop/labview.html (accessed 17/01/2022).
[45] Aldalur E, Veiga F, Suárez A, Bilbao J, Lamikiz A. High deposition wire arc additive manufacturing of mild steel: strategies and heat input effect on microstructure and mechanical properties. J Manuf Process 2020;58:615–26.
[46] Colegrove PA, et al. Microstructure and residual stress improvement in wire and arc additively manufactured parts through high-pressure rolling. J Mater Process Technol 2013;213(10):1782–91.
[47] Javadi Y, Akhlaghi M, Najafabadi MA. Using finite element and ultrasonic method to evaluate welding longitudinal residual stress through the thickness in austenitic stainless steel plates. Mater Design 2013;45:628–42.
[48] Vázquez L, Rodríguez N, Rodríguez I, Alberdi E, Álvarez P. Influence of interpass cooling conditions on microstructure and tensile properties of Ti-6Al-4V parts manufactured by WAAM. Welding in the World 2020;64(8):1377–88.
[49] Lines D, et al. Modelling of echo amplitude fidelity for transducer bandwidth and TFM pixel resolution. In: 47th Annual Review of Progress in Quantitative Nondestructive Evaluation; 2020.
[50] Zimermann R, et al. Implementation of an ultrasonic total focusing method for inspection of unmachined wire+ arc additive manufacturing components through multiple interfaces. In: 47th Annual Review of Progress in Quantitative Nondestructive Evaluation; 2020.